



Energy Efficiency Limit in CO-to-Ethylene Electroreduction and the Method to Advance Toward

Jin Zhang, Haoyang Jiang, Xiaotong Zhao, Zhaoyang Liu, Le Li, Weiping Ding, and Miao Zhong*

Abstract: The electrified synthesis of high-demand feedstocks (C_2H_4) from CO and H_2O through a CO electroreduction (COR) protocol is attractive for large-scale applications; however, a high reaction potential and modest Faradaic efficiencies (FEs) limit its practical energy efficiency (EE). In this study, a quantitative reaction–transport model was constructed to analyze the root causes of low performance in COR, which revealed low volumetric exchange current density and limited intermediate surface reaction as key factors, constraining CO-to- C_{2+} and CO-to- C_2H_4 conversion energetics and selectivities. Consequently, a robust, high active-site density electrode, featuring nanometer-scale interspacing between the active, Nafion-wrapped Cu^{+} –Cu nanosheet catalysts, was designed. This design increases volumetric COR activity with an efficient intermediate surface reaction mechanism for C_2H_4 production, substantially lowering the full-cell COR potential to 1.87 V at 4 A in a 25 cm^2 membrane electrode assembly, thereby achieving a record >50% C_{2+} EE with a $90 \pm 1\%$ FE along with a >40% C_2H_4 EE with a $71 \pm 1\%$ FE throughout stable >100 h operation. Similarly designed high-volumetric-activity Bi and Ag nanosheet catalysts enabled >60% and >55% EEs for the CO_2 -to-formate and CO_2 -to-CO electroreduction, demonstrating the broader applicability of our electrochemical activity and EE enhancement concept on a three-phase interface.

Introduction

Short-chain C_2 – C_3 alkenes and alcohols, such as ethylene (C_2H_4), ethanol, and propanol, are in high demand because they are pivotal compounds in industrial chemical synthesis. In particular, the global production of C_2H_4 is projected to increase to 287 million tons by 2030, respectively, with a market value of \$245 billion.^[1] Traditional production methods rely heavily on finite fossil fuels and complex thermocatalytic processes, consuming a substantial amount of global annual energy and significantly contributing to global CO_2 emissions.^[2]

Therefore, the renewable-powered electrosynthesis of C_2H_4 from relatively low-cost CO and H_2O has emerged as a low-carbon-footprint alternative.^[3–5] This electrochemical process is thermodynamically uphill ($CO + H_2O \rightarrow C_2H_4 + O_2$, $\Delta_f G^\circ = 817.4 \text{ kJ mol}^{-1}$) and uses electrical

energy to drive chemical production. When conducting in an energy-intensified membrane electrode assembly (MEA) system, this electrochemical process delivers industrially relevant current densities of >100 mA cm^{-2} at the cathode and a C_2H_4 productivity comparable to that of thermal catalysis, while generating only O_2 at the anode under mild conditions.^[6,7] In addition, the Anderson–Schulz–Flory distribution does not apply to the electrochemical synthesis in this system because the reaction mechanism and pathways are different from those in thermal catalysis, which facilitates a high electrosynthesized C_2H_4 selectivity beyond that of the traditional Fischer–Tropsch limit.^[2]

Operating the CO electroreduction (COR) process in strong alkaline electrolytes (3–7 M KOH) has proven effective for the CO-to- C_{2+} conversion while suppressing the competing hydrogen evolution reaction (HER).^[8] This alkaline CO electrolysis process avoids the carbonate formation issue, offering an enhanced carbon utilization efficiency compared to that of the alkaline CO_2 electroreduction.^[9–12] The use of FeNi-based electrocatalysts for the alkaline oxygen evolution reaction (OER) at the anode further enables a low-cost device profile.

In this context, enhancing the energy efficiency (EE) and Faradaic efficiency (FE) of MEA-based CO-to- C_{2+} and CO-to- C_2H_4 electrosynthesis protocols is central to advancing this technology; nonetheless, it remains a significant challenge. Although recent efforts in electrocatalyst development and electrolyte engineering have raised the CO-to- C_2H_4 FE to >65%,^[13–15] their high operating potentials in the range of 2.3–3.1 V substantially constrain the full-cell EE for practical applications (Table S1).

[*] J. Zhang, H. Jiang, X. Zhao, Z. Liu, L. Li, M. Zhong

College of Engineering and Applied Sciences, National Laboratory of Solid State Microstructures, the Frontiers Science Center for Critical Earth Material Cyclings, Collaborative Innovation Center of Advanced Microstructure, Nanjing University, No. 163, Xianlin Avenue, Qixia District, Nanjing 210023, China
E-mail: miaozhong@nju.edu.cn

W. Ding
School of Chemistry and Chemical Engineering, Nanjing University, No. 163, Xianlin Avenue, Qixia District, Nanjing 210023, China

Additional supporting information can be found online in the Supporting Information section

The above shortfalls can be partially attributed to an incomplete understanding of the intricate COR kinetics at electrode/CO/electrolyte interfaces, and more critically, to the absence of effective methods for improving energy and mass transfer to achieve breakthroughs in EE and FE at high current densities with minimal potential losses during electrosynthesis.^[16–26] Further, the selectivity mechanisms for COR to a single C₂₊ product remain elusive. Although the COR EE and selectivity mechanisms are closely related, i.e., both are influenced by reaction energies on the active sites and the surrounding environment at the three-phase interface, these mechanisms differ significantly. More specifically, EE operates on a purely energetic scale, encompassing only the energy requirements for reaction and reactant transport, whereas the selectivity depends on the competition between the kinetics of different reaction pathways, wherein the local environments critically shape the intermediate concentrations that determine the product selectivity.^[27–30] This intrinsic distinction has led to a gap in unified and systematic studies improving both aspects. Specifically, no quantitative reaction-transport model grounded in solid experimental results is available for analyzing these critical energy and selectivity requirements across different scales. Such a model is vital for guiding the design of catalyst three-phase interfaces and electrode structures to maximize the efficacy of each active COR site. For example, attaining energy-efficient and selective CO-to-C₂₊ and CO-to-C₂H₄ processes necessitate a full-cell potential below 2.0 V (a critical value for achieving >40% EE at an estimated 75% product FE, with 40% EE being calculated as the profitable benchmark for electrochemical COR to chemicals at current electricity price)^[14] at an industrial current density of >100 mA cm⁻².

With these considerations in mind, we report the development of a quantitative reaction-transport framework that decouples the COR EE and FE with regards to the kinetics and reaction pathways. Two critical descriptors are identified (i.e., $(i_0 S^*/\rho_{lq})^{-1/2}$ and $1 - \exp(-b/S^*)$), which incorporate the volumetric exchange current density ($i_0 S^*$), the volumetric resistance (ρ_{lq}), and the structure-induced intermediate surface retention (proportional to the volumetric specific surface area S^*) as key factors in governing the COR-to-C₂H₄ energetics and selectivity. A highly active electrosynthetic nanonetwork was designed by leveraging model insights. This nanonetwork features a high volumetric density of active sites and nanometer scale intersite spacing integrated within an efficient reaction and transport framework. The developed system significantly enhances the EEs and selectivities of the CO-to-C₂₊ and CO-to-C₂H₄ electrosynthesis processes. More specifically, highly active, Nafion-wrapped Cu⁺-Cu interface catalysts are prepared to accelerate the *CO-*CO coupling kinetics in the presence of high-K⁺-concentration electrolytes. Subsequently, these highly active NSs catalysts are densely packed in a stratified, 2-μm-thick porous electrode (PTFE@C/Nafion@Cu₂O-Cu NSs/Cu/PTFE) to produce an enhanced volumetric active site density (PTFE, polytetrafluoroethylene). The full-cell COR potential for this system is subsequently evaluated, and the CO-to-C₂₊ EE is determined. Further, the effect of the self-assembled, nanometer-scale reaction spacing between the active sites

for facilitating an intermediate surface reaction mechanism is examined, and the impact of carbonate addition to the alkaline electrolyte on stabilizing the active sites *in situ* is investigated. Finally, this strategy is applied in the fabrication of high volumetric site density Bi and Ag NS electrodes, and their full-cell EEs in the CO₂ electroreduction reactions to produce formate and CO are determined to demonstrate the potential applicability of the described concept to different electrocatalysis systems.

Results and Discussion

Figure 1a summarizes the reported and our achieved EEs for CO-to-C₂H₄ and CO-to-C₂₊ electroreduction, along with our achieved current density versus full-cell voltage ($j-V$) performance. A commercial NiFeO_x anode (dioxide materials), which delivers an optimized voltage drop of 0.2–0.35 V at operating current densities of 100–200 mA cm⁻², and a commercial anion exchange membrane (FAA-3-50, FuMA Tech), which introduces an ohmic resistance-related potential loss of ~0.1 V within the same current density range, yields the maximum full-cell COR EE of 68–70%, assuming no energy loss at the cathode with a theoretical 100% FE.

Achieving this EE limit requires developing electroactive sites with fast COR kinetics and high COR FE at low overpotentials. More critically, when the high EE must align with commercially relevant current densities, for instance >100 mA cm⁻², simply improving the intrinsic activity on the individual site becomes insufficient. Instead, it is necessary to integrate the high-activity single site into a high-site-density reaction-transport framework that couples efficient energetics and multisite-synergy selectivity mechanisms spanning molecular-scale reactions to mesoscopic transport. Establishing quantitative correlations with descriptors to characterize EE and FE performance at high current densities is imperative for guiding further advancements.

Given these considerations, we started with evaluating the CO-to-C₂H₄ overpotential by varying electrocatalysts, surface ionomers, and reaction electrolytes. This aims to identify the most electroactive individual site and its local reaction environment as an intrinsic site activity to achieve rapid reaction kinetics for the CO-to-C₂H₄ electrosynthesis protocol. To this end, the CO-to-C₂H₄ onset potentials were assessed in 1–7 M KOH and 3 M KF electrolytes for a range of Cu-based catalysts coated with different surface ionomers (Figure S1). Among these catalysts, Nafion-wrapped Cu⁺-Cu interface catalysts (denoted Nafion@Cu₂O-Cu) demonstrated a notably low onset potential of −0.08 V_{RHE} for C₂H₄ production. Replacing Nafion with an anion-exchange ionomer shifted the C₂H₄ onset potential to be more cathodic (−0.33 V_{RHE}), indicating that a highly active Cu⁺-Cu interface catalyst and a high local K⁺ concentration favor the CO-to-C₂H₄ and CO-to-C₂₊ conversion kinetics.

We design a robust nanonetwork electrode structure featuring the Nafion@Cu⁺-Cu interface catalysts densely packed within a confined space (denoted Nafion@Cu₂O-Cu NSs) (Figure 1b) to enhance the CO-to-C₂H₄ and CO-to-C₂₊ EEs at the high activity region. This design achieves

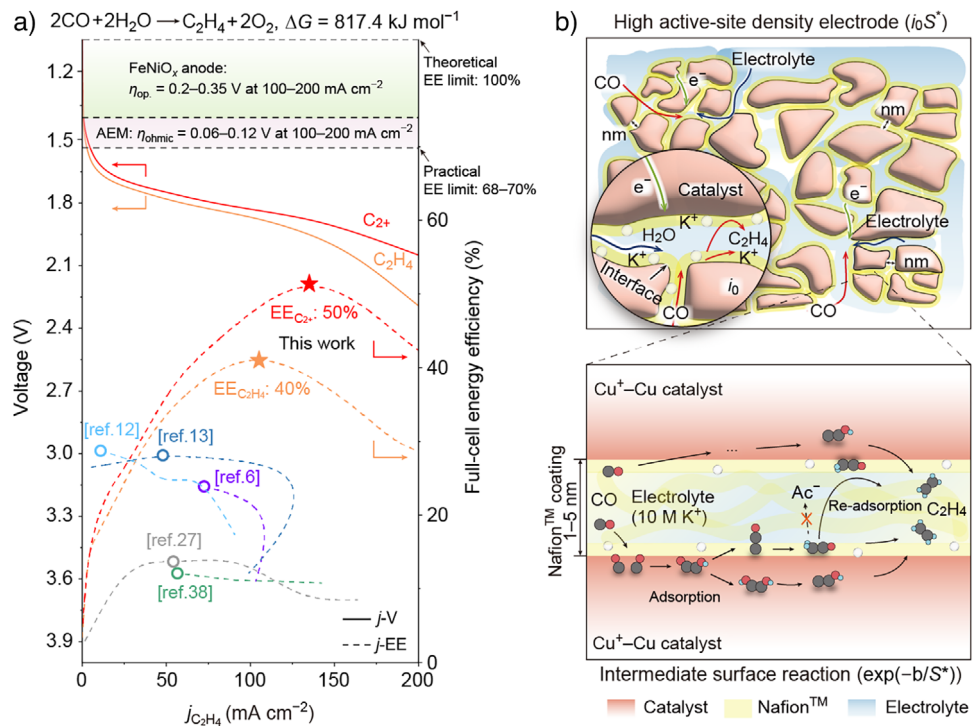


Figure 1. Constructing high active-site density nanonetwork gas diffusion electrode with a dynamic surface reaction mechanism. a) Summary of the reported EEs for the CO-to- C_2H_4 electroreduction and our achieved EEs and j - V performance.^[6,12,13,27,31] b) Schematic illustration of the high active-site density nanonetwork electrode model and the dynamic intermediate surface reaction of the C_2H_4 formation pathway.

a high volumetric active site density to concentrate the produced intermediates and promote the COR with reduced energy losses. The nanometer-scale channels between the active sites facilitate an intermediate adsorption–desorption–readsorption surface reaction mechanism.^[32] In addition, the presence of hydrophobic Nafion ionomer within these channels suppresses the reaction of ${}^*\text{CCO}$ and ${}^*\text{H}_2\text{CCO}$ with water/ OH^- to produce Ac^- , thereby that selectively favoring pathways leading to C_2H_4 production (Figure 1b). Further, the surface Nafion ionomer coating facilitates the efficient transport of CO and K^+ to electrocatalyst surfaces, thereby enhancing energy-efficient CO-to- C_2H_4 electrosynthesis.

To validate the EE-enhancement concept, various catalysts were synthesized containing the same $\text{Cu}^+ - \text{Cu}$ active sites by varying volumetric active-site densities (Figures S2 and S3), and their performances were evaluated in different KOH and KF electrolytes. Consequently, a descriptor was identified (i.e., $(i_0\text{S}^*/\rho_{\text{iq}})^{-1/2}$), wherein S^* is volumetric surface active area and indicates the catalyst active-site density, i_0 is the exchange current density and indicates the site activity, and ρ_{iq} is the specific ohmic resistance for electron and ion transport. This descriptor is inversely correlated with the CO-to- C_{2+} EE, as plotted in Figure 2a and expressed by Equation (1) (see Supporting Information for a detailed derivation and explanation):

$$\text{EE}_{\text{C}_{2+}} = \frac{1}{(E^\theta)^{-1} I_{\text{total}} \left(\frac{nF}{RT}\right)^{-1/2} \left(\frac{i_0\text{S}^*}{\rho_{\text{iq}}}\right)^{-1/2} + \frac{V'}{E^\theta}} \times \text{FE}_{\text{C}_{2+}} \quad (1)$$

where E^θ represents the thermodynamic reaction potential of different C_{2+} products, n represents the number of moles, F represents the Faraday's constant, R represents the gas constant, T represents the Kelvin temperature, $\text{FE}_{\text{C}_{2+}}$ represents FE of different C_{2+} products, and V' represents the algebraic sum of other overpotential parameters besides the cathode overpotential.

Equation (1) confirms that increasing the overall volumetric active-site density (S^*) with rapid C–C coupling kinetics at each active site (i_0) is necessary for enhancing the CO-to- C_{2+} energetics (Figure 2a).

Following C–C coupling, there is no reaction barrier for individual C_{2+} production at a cathodic potential, which means that improving the energetics at the individual active sites will not lead to selectivity control. The selectivities toward the two major alkaline COR products, C_2H_4 and acetate (Ac^-), depend on the intermediate concentrations and their distinct reaction pathways; C_2H_4 formation relies on surface-binding ketene (${}^*\text{CCO}$ and ${}^*\text{H}_2\text{CCO}$) intermediates migrating across the catalyst surface for hydrogenation,^[32] while Ac^- forms when these ketene intermediates desorb and react with the OH^- species of the alkaline electrolyte (Supporting Information).^[33] A “selectivity factor” is also identified to describe divergent pathways (i.e., $1 - \exp(-b/S^*)$), which reflects the Ac^- intermediate concentration in the electrolyte through the incorporation of intermediate desorption kinetics following Fick's second law of diffusion and accounts for the relevant geometrical effects, as outlined in

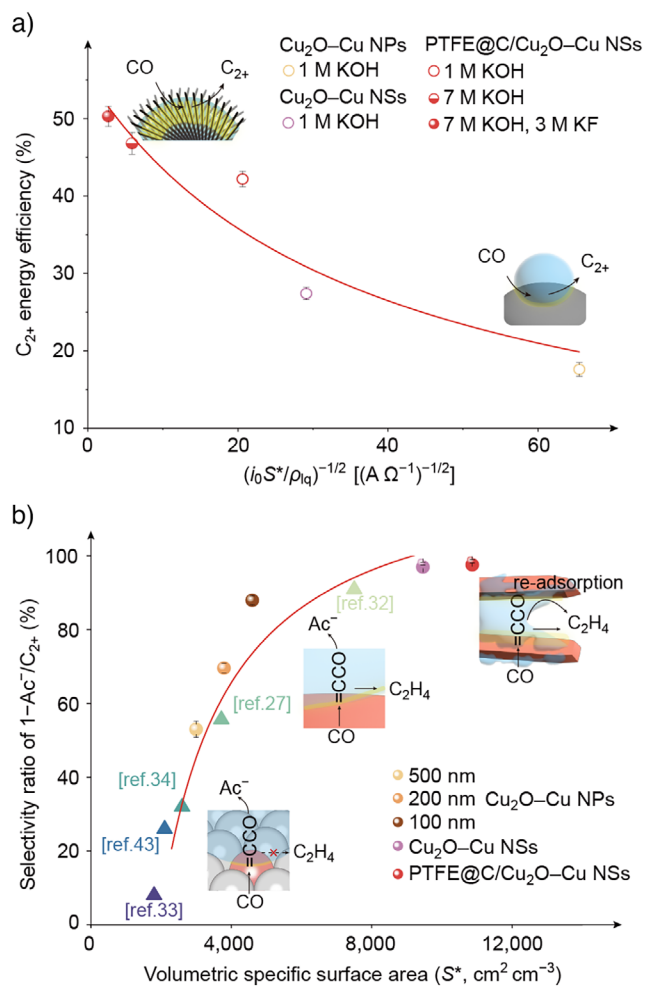


Figure 2. Quantitative correlations to describe energy efficiency (EE) and selectivity. a) Full-cell C_{2+} EEs obtained using different CuO-derived catalyst electrodes. The x-axis indicates the square root of the ratio of the volumetric exchange current density ($i_0 S^*$) to the solution resistance (ρ_{iq}). b) Acetate (Ac^-) selectivity in the C_{2+} product and a comparison with previously reported results.^[27,33–36] Different CuO-derived catalyst electrodes ($\text{Cu}_2\text{O}-\text{Cu NPs}$ with different particle sizes (100, 200, and 500 nm), $\text{Cu}_2\text{O}-\text{Cu NSs}$, and $\text{PTFE}@\text{C}/\text{Cu}_2\text{O}-\text{Cu NSs}$) were employed in 7 M KOH and 3 M KF electrolytes. The x-axis indicates the descriptor volumetric specific surface area (S^*) for the active-site densities of the different CuO-derived catalyst electrodes. The error bars in (a) and (b) represent the standard deviations based on three independent measurements.

Equation (2):

$$Sel_{\text{Ac}^-} = \frac{K_{\text{ads-des}} \sqrt{D_{\text{H}_2\text{CCO}} k_{\text{Ac}^-} [\text{OH}^-]}}{k_{\text{des}} + k_{\text{hyd}} [\text{H}^+]} \left(1 - e^{-\sqrt{\frac{k_{\text{Ac}^-} [\text{OH}^-]}{D_{\text{H}_2\text{CCO}}}}} x \right) \quad (2)$$

where x represents the diffusion-limited distance of the ketene intermediate, which is inversely proportional to S^* . A detailed derivation and explanation of Equation (2) is presented in Supporting Information.

Figure 2b reveals an exponential relationship between $1/S^*$ and the Ac^- selectivity (represented by $1-\text{Ac}^-/\text{C}_{2+}$) on the Cu^+-Cu catalyst, which indicates the need to design catalysts with nanometer-scale spacing channels that can facilitate intermediate surface reaction mechanism on the catalyst (Figure 1b). Such a design can increase intermediate retention on the surface to promote C_2H_4 formation while suppressing Ac^- production. Thus, $\text{Cu}_2\text{O}-\text{Cu NSs}$ are densely incorporated into a stratified composite electrode structure with an exceptionally high volumetric active-site density (S^*) of $11\,000 \text{ cm}^2 \text{ cm}^{-3}$, achieving an Ac^- FE of $<2\%$ in a 7 M KOH/3 M KF electrolyte. This represents a significant reduction from the typical Ac^- FEs of 20–30% commonly obtained in such strongly alkaline environments. Consequently, C_2H_4 , ethanol, and propanol FEs exceeded 90%, with the C_2H_4 FE alone surpassing 71%. This selectivity model reconciles previous findings into the selectivities toward Ac^- and C_2H_4 (Figure 2b). For example, Sargent et al. reported that atomic-level Cu doping in Ag weakened ketene adsorption kinetics, while Kang et al. showed that large, flattened Cu catalysts ($>1.7 \mu\text{m}$) increased catalyst-electrolyte contact. In these cases, the Ac^- FEs were promoted to $>90\%$ and 70%, respectively.^[34,35]

Figure 3a–c provides a schematic and cross-sectional scanning electron microscopy (SEM) images of the stratified electrode. The bottom layer consists of a 500-nm-thick Cu layer sputtered on PTFE, which serves as an efficient electrical current collector while maintaining a suitable hydrophobicity for fast CO diffusion (Figure S4). The $1.5\,\mu\text{m}$ -thick catalyst layer consists of Nafion@ $\text{Cu}_2\text{O}-\text{Cu}$ NSs exhibiting 300–700 nm interconnected pores (Figure 3c). A 3D reconstruction of the Nafion@ $\text{Cu}_2\text{O}-\text{Cu}$ NS catalyst layer using focused ion beam SEM (FIB-SEM) revealed a well-defined porous network with porosity exceeding 45% (Figure S5). Simulations confirmed that CO diffusion within these large pores was sufficient, maintaining a stable CO concentration of $>38 \text{ mM}$ for a pore size exceeding 100 nm at current densities of $50\text{--}400 \text{ mA cm}^{-2}$ (Supporting Information and Figure S6). Flow cell experiments validated these simulations, demonstrating that the saturated COR current density increased to $>300 \text{ mA cm}^{-2}$ at a cathodic potential of $-0.5 \text{ V}_{\text{RHE}}$ (Figure 3f).

A hydrophobic PTFE-wrapped carbon nanoparticle (PTFE@C) layer was introduced on top of the catalysts (Figure S7) to prevent electrolyte flooding and maximize the three-phase interface for the COR process. This PTFE@C layer enhanced the hydrophobicity of the electrode, increasing the water contact angle from 93.3° to 145° without compromising the underlying electrical conductivity (Figure S8). Comprehensive analyses were performed to examine the three-phase COR areas and the electrolyte conductivity within the optimized electrode structure, and the results are presented in Figures S9–S12.

A diffusion-type reaction–transport model was then built to study the operational potential losses caused by ion/electron/CO transport within the stratified cathode. Considering that COR was found to occur at dispersed three-phase interfaces throughout the electrode, collecting each separated COR current from different parts in the

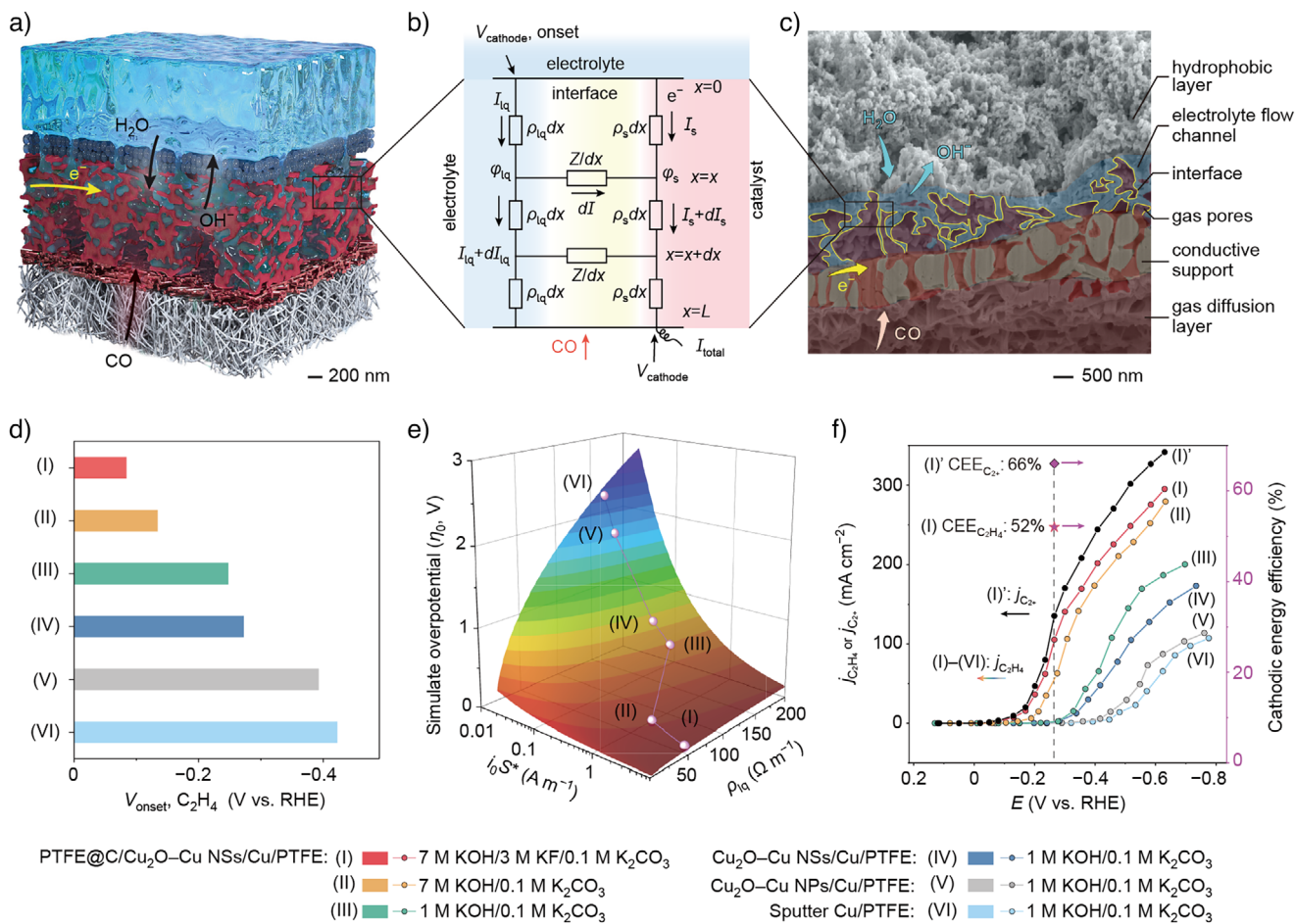


Figure 3. Energy contributions in a stratified PTFE@C/Nafion@Cu₂O-Cu NSs/Cu/PTFE electrode during COR. a) Schematic representation of the PTFE@C/Nafion@Cu₂O-Cu NSs/Cu/PTFE electrode structure. b) Equivalent electrical circuit diagram. c) Cross-sectional focused ion beam-scanning electron microscopy (FIB)-SEM image of the PTFE@C/Nafion@Cu₂O-Cu NSs/Cu/PTFE electrode. d) C_2H_4 onset potentials of the different electrode structures and electrolytes determined from the Tafel plots. e) Simulated overpotential results at 100 mA cm^{-2} C_2H_4 partial current density using a diffusion-type reaction-transport analytical model. $i_0 S^*$ and ρ_{iq} represent the volumetric COR exchange current density and the specific electrolyte resistance per unit length in the different cathodes. f) C_2H_4 partial current densities and cathodic COR energy efficiencies using different electrodes and electrolytes. Black line: C_{2+} partial current densities. Star and rhombus symbols: cathodic C_2H_4 and C_{2+} EEs for COR at a 100 mA cm^{-2} C_2H_4 partial current density.

electrode led to energy loss. This was attributed to the electrical resistance in the catalyst layer, along with the electrolyte resistance for OH^- transport out of the composite membrane-electrode. The equivalent electrical circuit used to calculate the operational potential loss at the cathode is shown in Figure 3b. The relationship between the current (I_{total}) and operational-potential loss (η_0) of the electrode can be expressed as:^[37]

$$I_{\text{total}} = \eta_0 \left(\frac{nF}{RT} \frac{i_0 S^*}{\rho_{\text{iq}}} \right)^{1/2} \quad (3)$$

where $i_0 S^*$ and ρ_{iq} represent the two critical descriptors presented above (Figures 3e and S13). Further details are provided in Supporting Information.

As shown in Figure 3e, overpotential simulations were conducted at the same current density of 100 mA cm^{-2} for different catalysts and electrolytes. When employing sputtered Cu as a catalyst and 1 M KOH/0.1 M K_2CO_3

as the electrolyte, the overpotential reached 2.3 V due to a minimal $i_0 S^*$ of 0.02 A m^{-1} . A modest reduction in the overpotential was observed upon coating the Cu/PTFE with commercial CuO nanoparticles (NPs). A marked decrease in the COR operating potential was observed when using Cu₂O-Cu NSs as the catalyst, suggesting that faster catalysis occurred over the Cu₂O-Cu NSs due to the improved COR kinetics resulting from increased reaction areas. A second notable decrease in the operating potential was observed using the 7 M KOH/3 M KF/0.1 M K_2CO_3 electrolyte. This originated from a pronounced reduction in the electrolyte resistance (reducing ρ_{iq} to $51 \Omega \text{ m}^{-1}$), which facilitated the rapid transport of ions within the $\sim 2\text{-}\mu\text{m}$ -thick electrode. Overall, the PTFE@C/Nafion@Cu₂O-Cu NSs/Cu/PTFE catalyst exhibited a significantly higher $i_0 S^*$ value of 6.8 A m^{-1} compared to the corresponding values of 0.17 and 0.03 A m^{-1} recorded for the uncoated Cu₂O-Cu NSs and Cu₂O-Cu NPs. These efforts yielded a remarkably low potential loss, and the C_2H_4 and C_{2+} cathodic

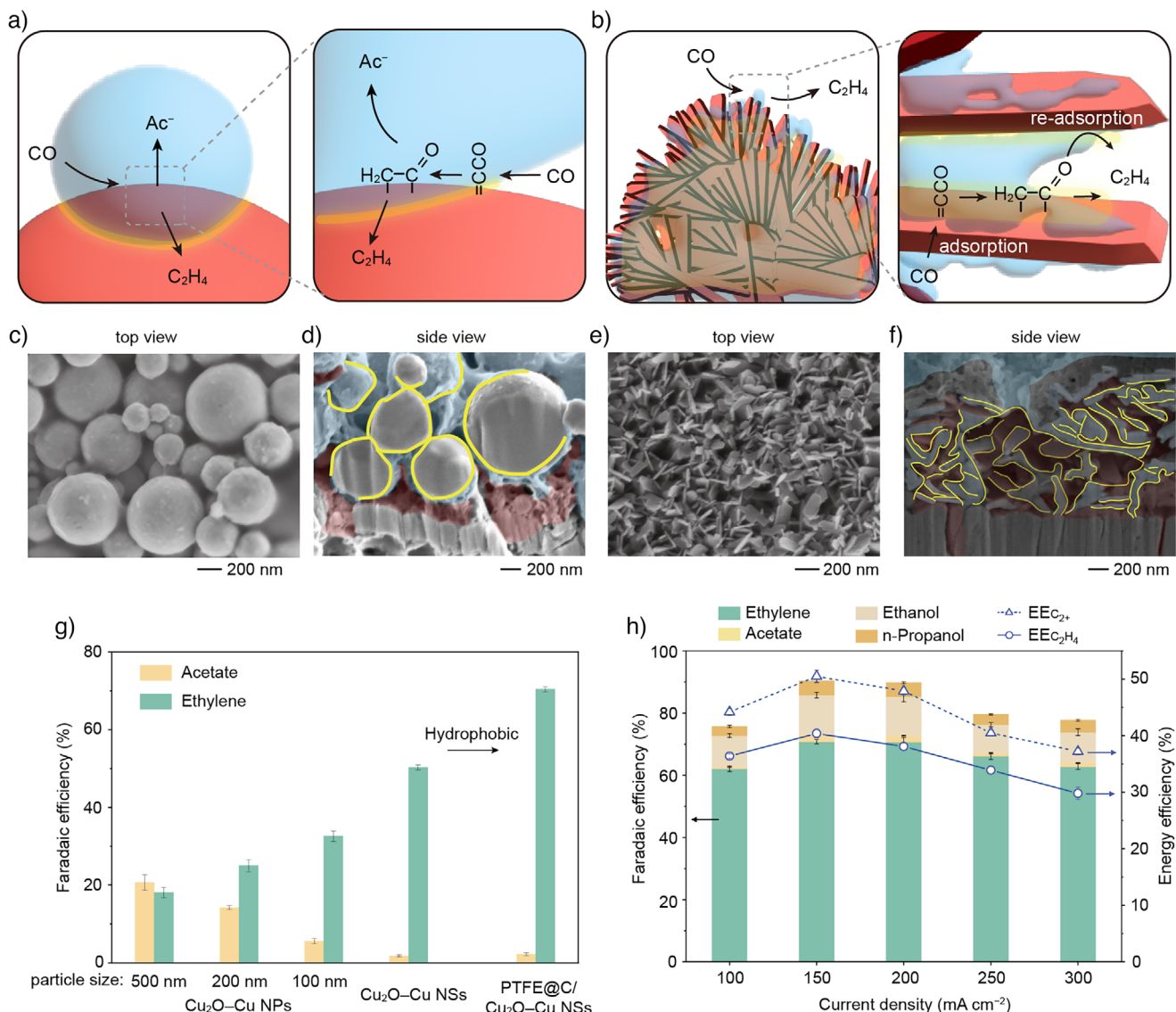


Figure 4. Selectivity analysis of the CO-to-C₂₊ products on the Nafion-wrapped CuO-derived Cu₂O–Cu catalyst electrodes with different morphologies. a), b) Schematic illustrations of the CO-to-C₂H₄ and CO-to-acetate reactions on a) Cu₂O–Cu NPs and b) Cu₂O–Cu NSs electrodes. c)–f) SEM and FIB-SEM images of the c), d) Cu₂O–Cu NPs with a particle size of 500 nm and e), f) the Cu₂O–Cu NSs electrodes. The yellow solid lines indicate the reaction interface. g) FEs of the acetate and C₂H₄ products obtained using Cu₂O–Cu NPs with different particle sizes (100, 200, and 500 nm), Cu₂O–Cu NSs, and PTFE@C/Cu₂O–Cu NSs. h) FEs and full-cell EEs for C₂H₄ (solid lines) and C₂₊ (dashed lines) at 100–300 mA cm⁻² in 7 M KOH/3 M KF/0.1 M K₂CO₃ electrolytes with PTFE@C/Nafion@Cu₂O–Cu NSs/Cu/PTFE electrode. The error bars in g) and h) represent the standard deviation based on three independent measurements.

EEs reached 52% and 66%, respectively (Figure 3d–f), ultimately outperforming previous electrocatalytic systems (Table S2).

To study the relationship between catalyst morphology and the product selectivity, the COR performances were compared for the Nafion@Cu₂O–Cu NSs and NPs with varying particle sizes. Figures 4a–f and S3,S14–S16 show the morphologies of the different catalysts. The NSs possess abundant nanometer-scale channels (30–300 nm) with Nafion included that allow *CCO and *H₂CCO to be retained on the surface (adsorption) and facilitate intermediate reattachment from the electrolyte phase (desorption–readsortion)

between the active site surfaces, thereby enhancing C₂H₄ selectivity.

In the 7 M KOH electrolyte, the stacked Nafion@Cu₂O–Cu NS electrode demonstrated a C₂H₄ FE of >50% at 150 mA cm⁻². Furthermore, the more hydrophobic PTFE@C/Nafion@Cu₂O–Cu NSs/Cu/PTFE electrode resulted in a C₂H₄ FE of 71%, while the Ac[–] FE was <2% (Figure 4g,h and Table S3). In contrast, 500 nm Nafion@Cu₂O–Cu NPs with large intersite spacings exhibited significantly higher Ac[–] FEs, exceeding 20%. These results validate our proposed intermediate surface reaction mechanism on catalysts for enhanced C₂H₄ synthesis.

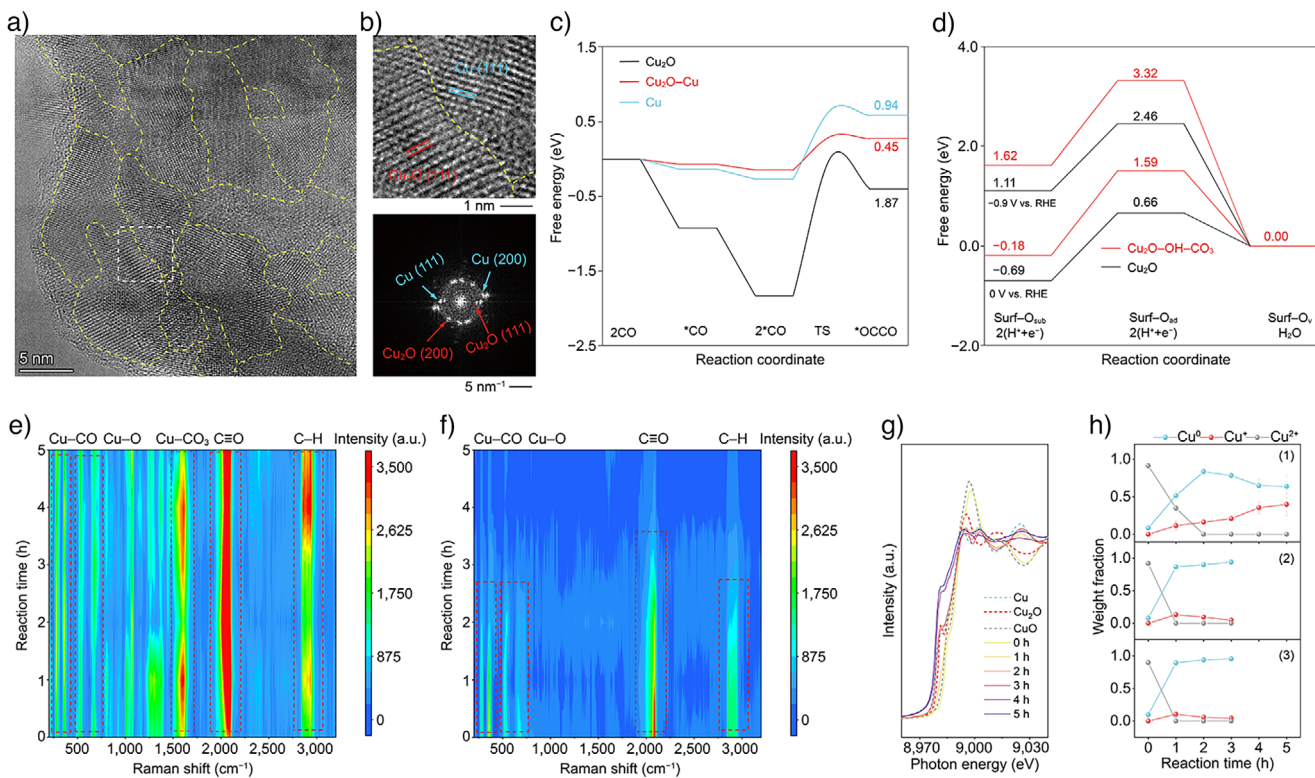


Figure 5. Structural characterization and chemical state analysis of the CuO-derived catalysts during COR. a) HR-TEM image of the CuO-derived catalyst after a 150 h COR process at 150 mA cm⁻² in the 1 M KOH/0.1 M K₂CO₃ electrolyte. b) Magnified HR-TEM image of the white region in (a), along with the corresponding FFT patterns. The yellow-dashed lines indicate the Cu₂O-Cu interfaces. c) Energy diagram depicting the reaction energy of *CO-*CO coupling at the Cu₂O-Cu interface (red) and the pure Cu₂O (black) and Cu (cyan) surfaces. d) Energy diagram depicting the reaction pathway from O_{sub} to O_v on the Cu₂O-OH (black) and Cu₂O-CO₃-OH (red) surfaces. e), f) In situ Raman spectra recorded during the 5 h COR at 150 mA cm⁻² in e) 1 M KOH/0.1 M K₂CO₃ and f) 1 M KOH electrolytes. g) In situ Cu K-edge XANES spectra for the PTFE@C/Nafion@Cu₂O-Cu NSs/Cu/PTFE system at 150 mA cm⁻² over varying times during COR. h) Time-dependent curves detailing the fractions of the Cu chemical states under varying conditions: (1) PTFE@C/Nafion@Cu₂O-Cu NSs in 1 M KOH/0.1 M K₂CO₃, (2) Nafion@Cu₂O-Cu NSs in 1 M KOH/0.1 M K₂CO₃, and (3) PTFE@C/Nafion@Cu₂O-Cu NSs in 1 M KOH.

Ex situ and in situ characterization was performed before, during, and after the COR process to investigate the material and microstructural properties of the Nafion@Cu₂O-Cu NSs catalyst. The photographic and SEM and cross-sectional images (Figure S17) show a distinctive NS morphology for the hydrothermally synthesized CuO sample, with an average thickness, width, and length of 20, 200, and 1000 nm, respectively. This NS morphology remained stable following a continuous 150 h COR process at 150 mA cm⁻². In addition, the transmission electron microscopy (TEM) images (Figure 5a,b) show abundant Cu (111), Cu (200), Cu₂O (111), and Cu₂O (200) facets with sizes of ~5–30 nm after the 150 h COR reaction. TEM, X-ray diffraction patterns, and X-ray photoelectron spectroscopy revealed that the initial monoclinic CuO NS crystal structure was completely transformed into a polycrystalline mixture of cubic Cu₂O (Pn-3m) and cubic Cu (Fm-3m) nanocrystals after the 150 h process (Figures S17–S19).^[18,22] Notably, such polycrystalline surfaces with enriched Cu₂O-Cu nanofragment interfaces provide a high geometric density of catalytically active sites for CO adsorption and electroreduction.

Density functional theory (DFT) calculations revealed that the energy barrier for *CO-*CO coupling at the

Cu₂O-Cu (111) interface is significantly lower (0.45 eV) than those at the Cu (111) and Cu₂O (111) surfaces (0.94 and 1.87 eV, respectively), as shown in Figures 5c, S20 and Table S4. In situ Raman spectroscopy indicated the presence of stable Cu-O bonds (530 and 630 cm⁻¹) along with a carbonate (CO₃²⁻) stretching peak corresponding to the copper hydroxy carbonate moiety (1200–1800 cm⁻¹, Figure S21),^[38] and suggesting stabilization of the Cu⁺ species in Cu₂O through the formation of a carbonate-coordinated copper hydroxycarbonate on the CuO_x surface (Figure 5e). Simultaneously, representative intermediate peaks associated with Cu-CO (~280 and 370 cm⁻¹), C≡O (bridge-type: 1900–2000 cm⁻¹ and atop-type: 2000–2100 cm⁻¹), and C-H stretching (2800–3000 cm⁻¹)^[31,39,40] were consistently observed, indicating an active COR process over the Cu₂O-Cu NS catalyst. In contrast, in the carbonate-free 1 M KOH electrolyte, the Cu-O peaks disappeared, and the Raman peak intensities corresponding to the Cu-CO, C≡O, and C-H moieties decreased (Figure 5f), representing a reduction in the COR performance (Figure S22). Further, the DFT calculations indicated that the presence of OH⁻ and CO₃²⁻ species on the Cu₂O surface increases the energy barrier for O migration, mitigating Cu₂O reduction and stabilizing

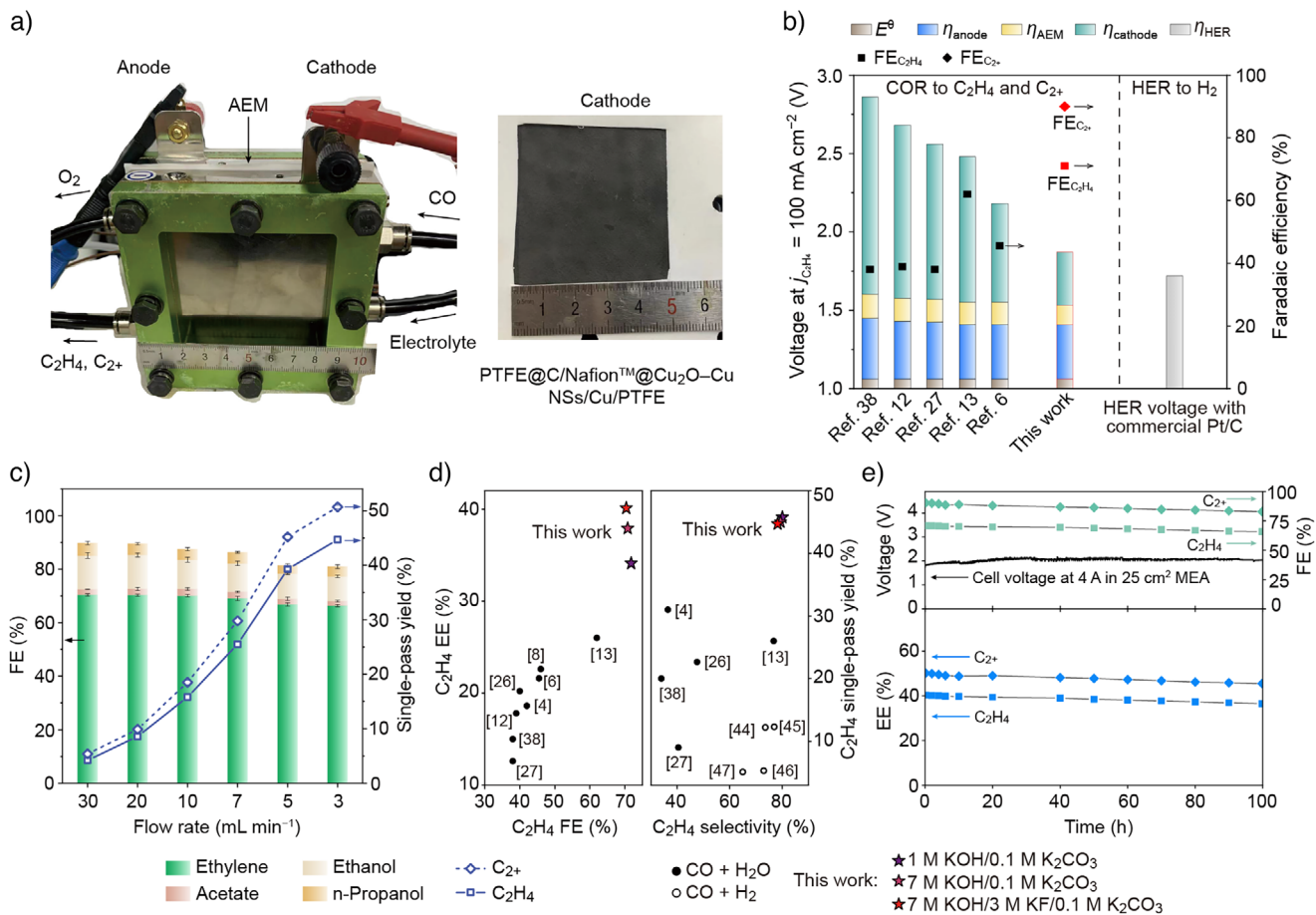


Figure 6. COR performance in a 25 cm² MEA electrolyzer with a PTFE@C/Nafion@Cu₂O–Cu NSs/Cu/PTFE electrode. a) Photographic images of the 25 cm² MEA electrolyzer and the PTFE@C/Nafion@Cu₂O–Cu NSs/Cu/PTFE cathode. b) Comparison of the full-cell potentials and the C₂H₄ FE for the COR at a C₂H₄ partial current density of 100 mA cm⁻².^[6,12,13,27,31] The brown, blue, yellow, and green bars represent the thermodynamic potential along with the anode, membrane, and cathode potentials. The gray bar represents the full-cell HER potential obtained using a commercial Pt/C cathode and IrO₂ anode.^[42] The red rhombus and the square symbols represent the C₂₊ and C₂H₄ FE obtained in the current work. c) FEs and single-pass yields for C₂H₄ (solid lines) and C₂₊ (dashed lines) at various CO flow rates and 150 mA cm⁻². d) Comparison of the C₂H₄ FE, single-pass C₂H₄ yield, and full-cell C₂H₄ EE with previous reports for the electrochemical (CO + H₂O, solid sphere) and thermocatalytic (CO + H₂, hollow sphere) synthesis (Tables S1 and S11).^[4,6,8,12,13,26,27,31,44–47] e) Stability results obtained using PTFE@C/Nafion@Cu₂O–Cu NSs/Cu/PTFE and a 7 M KOH/3 M KF/0.1 M K₂CO₃ electrolyte at 4 A in a 25 cm⁻² MEA.

the Cu₂O–Cu interface (Figures 5d, S23 and Supporting Information). This surface coordination passivation strategy aligns with previous reports,^[41] which describe that the presence of a binuclear [Cu(μ-HCOO)(OH)₂]₂ layer on the Cu surface prevents O₂ from penetrating and reacting with the subsurface Cu species, thereby preventing Cu corrosion in highly oxidizing environments. In situ X-ray absorption near edge structure (XANES) analysis showed that ~36% of the Cu⁺ content remained stable after a 5 h reaction in the 1 M KOH/0.1 M K₂CO₃ electrolyte (Figures 5g,h, S24 and Table S5), while in the carbonate-free electrolyte, the Cu⁺ content decreased to <5%.

The COR performance of the PTFE@C/Nafion@Cu₂O–Cu NSs/Cu/PTFE electrode was evaluated in a 5 cm² MEA equipped with a Fumasep FAA-3–50 anion-exchange membrane (AEM) and a commercial NiFeO_x/Ti anode (Figures S25,S26 and Tables S6–S8, Supporting Information), and in a scaled-up 25 cm² MEA (Figure 6a). Electrochemical

tests conducted in different electrolytes at 100–300 mA cm⁻² (Figures 4h and S27) showed a high C₂₊ FE of 90 ± 1% in the 7 M KOH/3 M KF/0.1 M K₂CO₃ electrolyte system at 150 mA cm⁻², with a 71 ± 1% FE being achieved for C₂H₄. Based on the potential distribution results presented in Figures S28–S30, it was apparent that the PTFE@C/Nafion@Cu₂O–Cu NSs catalyst demonstrates an onset potential of –0.08 V_{RHE} when converting CO to C₂H₄, which is significantly lower than the best previously reported CO and CO₂R onset potentials.^[6,7] In addition, at a C₂H₄ partial current density of ~100 mA cm⁻², cathodic potential was determined to be merely –0.25 V_{RHE}. This low cathodic potential for the 8-electron-transfer CO-to-C₂H₄ reduction is close to that reported for the 2-electron-transfer HER performed using a Pt/C electrode at the same current density (Figure 6b),^[42] indicating an improvement in the COR kinetics close to the cathodic limit. Figure S30 compares the $j_{\text{C}_2\text{H}_4} - V$ curve of the best-performing catalyst with previous

results.^[6] The full-cell potential appeared significantly lower across the C₂H₄ partial current density range of 10–200 mA cm⁻², representing up to 40% reductions compared to current state-of-the-art overpotentials. Furthermore, in a MEA at 150 mA cm⁻², the full-cell potential was only 1.87 V, and the full-cell C₂₊ EE (without *iR* compensation) reached 50 ± 1% with a 90 ± 1% C₂₊ FE, whereas the EE for C₂H₄ was 40 ± 1% with a 71 ± 1% C₂H₄ FE (Figures 6b and S30). These results are superior to the previously reported EE value of 26% with a C₂H₄-ethanol distribution similar to that of the current work (Table S9).^[13,43]

Single-pass yields of 50 ± 1% for C₂₊ and 45 ± 2% for C₂H₄ were achieved in a 25 cm² MEA at a 3 mL min⁻¹ CO flow rate, indicating a 1.25-fold increase in the C₂H₄ yield compared to the best current catalysts (Figure 6c,d and Tables S10,S11). The performance of COR was evaluated at different CO concentrations (Figure S31). The results showed that C₂H₄ and C₂₊ FEs did not decrease when using 30 and 60 vol% CO in Ar, indicating that the PTFE@C/Nafion@Cu₂O-Cu NSs/Cu/PTFE electrode was highly efficient and active for COR reaction. Notably, the C₂H₄ formation rate reached 13.1 mmol h⁻¹ at an increased CO flow rate of 30 mL min⁻¹ (Figure S32). A comparative analysis revealed a remarkable C₂H₄ yield and EE, outperforming previous electrocatalytic and thermal catalytic systems (Figure 6d).^[14] Further improvements are expected through the use of more active OER catalysts and conductive AEMs membranes.

This setup delivered a stable COR performance at an applied total current of 4 A (25 cm², Figure 6e). The performance reproducibility was confirmed with five independent tests using a 5 cm² MEA, each showing that the C₂H₄ and C₂₊ EEs consistently remained around their initial values over a 150 h continuous operation (Figure S33 and Table S12).

To validate this energy enhancement approach, Ag and Bi NSs assembled in stratified electrodes were fabricated, which were characterized by high volumetric site activities and site densities (Figure S34). Consequently, full-cell EEs of >55% and >60% were obtained in the CO₂-to-CO and CO₂-to-formate electroreduction processes (Figure S35 and Table S13), demonstrating the broad applicability of this approach in different electrocatalytic systems.

Conclusions

An efficient CO electroreduction (COR) protocol was achieved by developing an efficient and scalable system featuring high active-site density in a nanonetwork electrosynthesis space with nanometer spacings between active ionomer@Cu₂O-Cu interface active sites. This design significantly enhanced volumetric COR-to-C₂₊ activity (i_0S^*) and CO-to-C₂H₄ selectivity (1-exp($-b/S^*$)) protocols by establishing an efficient reaction-transport framework that coupled reaction energetics and selectivity mechanisms across scales. The developed highly active PTFE@C/Nafion@Cu₂O-Cu NSs/Cu/PTFE cathode substantially lowered the full-cell alkaline COR potential to 1.87 V at 150 mA cm⁻² and attained CO-to-C₂₊ and CO-to-C₂H₄ EEs of >50% and 40%, respectively, along with C₂₊ and C₂H₄ FEs exceeding 90%

and 70%, respectively, in a scaled-up 25 cm² membrane electrode assembly at a total current of 4 A. The operational stability was enhanced via a robust catalyst surface coordination passivation strategy. The two critical descriptors, namely (i_0S^*/ρ_{lq})^{-1/2} and 1-exp($-b/S^*$), were identified to establish quantitative correlations with the key features for catalyst and reaction system, including volumetric site density, site activity, intersite spacing. Consequently, this approach can be broadly applied to other complex, heterogeneous electrosynthesis methods for preparing valuable chemicals. Future work should focus on further reducing the reaction potential while also enhancing the electrocatalytic activity and selectivity for sustained operation in scaled-up devices.

Supporting Information

The authors have cited additional references within the Supporting Information.^[4,6–9,12,13,15,26,27,30,31,43,48–69]

Acknowledgements

This work was financially supported by the National Natural Science Foundation of China (grant number 22272078). The authors thank Dr. Lirong Zheng (Institute of High Energy Physics, Chinese Academy of Sciences) for his help in the XAS test, Prof. Dr. Edward H. Sargent for the valuable discussion, and Dr. Chenxi Guo for his valuable discussion of the DFT calculations.

Conflict of Interests

The authors declare no conflict of interest.

Data Availability Statement

The data that support the findings of this study are available from the corresponding author upon reasonable request.

Keywords: CO electroreduction • Energy efficiency • Ethylene • High active-site density • Reaction-transport framework

- [1] Global Ethylene Industry Outlook to 2025. Report No. GDCH0126ICR.
- [2] W. Li, H. Wang, X. Jiang, J. Zhu, Z. Liu, X. Guo, C. Song, *RSC Adv.* **2018**, *8*, 7651–7699.
- [3] M. Jouny, G. S. Hutchings, F. Jiao, *Nat. Catal.* **2019**, *2*, 1062–1070.
- [4] H. Li, P. Wei, T. Liu, M. Li, C. Wang, R. Li, J. Ye, Z.-Y. Zhou, S.-G. Sun, Q. Fu, D. Gao, G. Wang, X. Bao, *Nat. Commun.* **2024**, *15*, 4603.
- [5] Y. Liang, F. Li, R. Miao, S. Hu, W. Ni, S. Zhang, Y. Liu, Y. Bai, H. Wan, P. Ou, X.-Y. Li, N. Wang, S. Park, F. Li, J. Zeng, D. Sinton, E. H. Sargent, *Nat. Synth.* **2024**, *3*, 1104–1112.
- [6] A. Ozden, J. Li, S. Kandambeth, X.-Y. Li, S. Liu, O. Shekhah, P. Ou, Y. Zou Finfrock, Y.-K. Wang, T. Alkayyali, F. Pelayo García De Arquer, V. S. Kale, P. M. Bhatt, A. H. Ip, M. Eddaaoudi, E. H. Sargent, D. Sinton, *Nat. Energy* **2023**, *8*, 179.

- [7] C.-T. Dinh, T. Burdyny, M. G. Kibria, A. Seifitokaldani, C. M. Gabardo, F. P. García de Arquer, A. Kiani, J. P. Edwards, P. De Luna, O. S. Bushuyev, C. Zou, R. Quintero-Bermudez, Y. Pang, D. Sinton, E. H. Sargent, *Science* **2018**, *360*, 783–787.
- [8] W. Ren, W. Ma, X. Hu, *Joule* **2023**, *7*, 2349–2360.
- [9] J. Zhang, C. Guo, S. Fang, X. Zhao, L. Li, H. Jiang, Z. Liu, Z. Fan, W. Xu, J. Xiao, M. Zhong, *Nat. Commun.* **2023**, *14*, 1298.
- [10] M. Zhong, K. Tran, Y. Min, C. Wang, Z. Wang, C.-T. Dinh, P. De Luna, Z. Yu, A. S. Rasouli, P. Brodersen, S. Sun, O. Voznyy, C. S. Tan, M. Askerka, F. Che, M. Liu, A. Seifitokaldani, Y. Pang, S. C. Lo, A. Ip, Z. Ulissi, E. H. Sargent, *Nature* **2020**, *581*, 178–183.
- [11] J. E. Huang, F. Li, A. Ozden, A. Sedighian Rasouli, F. P. García de Arquer, S. Liu, S. Zhang, M. Luo, X. Wang, Y. Lum, Y. Xu, K. Bertens, R. K. Miao, C.-T. Dinh, D. Sinton, E. H. Sargent, *Science* **2021**, *372*, 1074–1078.
- [12] D. S. Ripatti, T. R. Veltman, M. W. Kanan, *Joule* **2019**, *3*, 240–256.
- [13] A. Ozden, Y. Wang, F. Li, M. Luo, J. Sisler, A. Thevenon, A. Rosas-Hernández, T. Burdyny, Y. Lum, H. Yadegari, T. Agapie, J. C. Peters, E. H. Sargent, D. Sinton, *Joule* **2021**, *5*, 706–719.
- [14] J. Sisler, S. Khan, A. H. Ip, M. W. Schreiber, S. A. Jaffer, E. R. Bobicki, C.-T. Dinh, E. H. Sargent, *ACS Energy Lett.* **2021**, *6*, 997–1002.
- [15] H. Wu, L. Huang, J. Timoshenko, K. Qi, W. Wang, J. Liu, Y. Zhang, S. Yang, E. Petit, V. Flaud, J. Li, C. Salameh, P. Miele, L. Lajaunie, B. Roldán Cuanya, D. Rao, D. Voiry, *Nat. Energy* **2024**, *9*, 422–433.
- [16] J. Li, D. Wu, A. S. Malkani, X. Chang, M.-J. Cheng, B. Xu, Q. Lu, *Chem. Int. Ed.* **2020**, *59*, 4464–4469.
- [17] L. Han, W. Zhou, C. Xiang, *ACS Energy Lett.* **2018**, *3*, 855–860.
- [18] F. Chen, Z.-C. Yao, Z.-H. Lyu, J. Fu, X. Zhang, J.-S. Hu, *eScience* **2024**, *4*, 100172.
- [19] R. Chen, H.-Y. Su, D. Liu, R. Huang, X. Meng, X. Cui, Z.-Q. Tian, D. H. Zhang, D. Deng, *Angew. Chem. Int. Ed.* **2020**, *59*, 154–160.
- [20] H. Zhang, J. Li, M.-J. Cheng, Q. Lu, *ACS Catal.* **2019**, *9*, 49–65.
- [21] H. Bao, Y. Qiu, X. Peng, J.-A. Wang, Y. Mi, S. Zhao, X. Liu, Y. Liu, R. Cao, L. Zhuo, J. Ren, J. Sun, J. Luo, X. Sun, *Nat. Commun.* **2021**, *12*, 238.
- [22] S. Sarfraz, A. T. Garcia-Esparza, A. Jedidi, L. Cavallo, K. Takanabe, *ACS Catal.* **2016**, *6*, 2842–2851.
- [23] W. Yang, H. Liu, Y. Qi, Y. Li, Y. Cui, L. Yu, X. Cui, D. Deng, *J. Energy Chem.* **2023**, *85*, 102–107.
- [24] X. Lu, T. Shinagawa, K. Takanabe, *ACS Catal.* **2023**, *13*, 1791–1803.
- [25] T. Alkayyali, M. Zargartalebi, A. Ozden, F. Arabyarmohammadi, R. Dorakhan, J. P. Edwards, F. Li, A. Shayesteh Zeraati, M. Fan, A. Bazylak, E. H. Sargent, D. Sinton, *Joule* **2024**, *8*, 1478–1500.
- [26] J. Li, Z. Wang, C. McCallum, Y. Xu, F. Li, Y. Wang, C. M. Gabardo, C.-T. Dinh, T.-T. Zhuang, L. Wang, J. Y. Howe, Y. Ren, E. H. Sargent, D. Sinton, *Nat. Catal.* **2019**, *2*, 1124–1131.
- [27] M. Jouny, W. Luc, F. Jiao, *Nat. Catal.* **2018**, *1*, 748–755.
- [28] Y. Pang, J. Li, Z. Wang, C.-S. Tan, P.-L. Hsieh, T.-T. Zhuang, Z.-Q. Liang, C. Zou, X. Wang, P. De Luna, J. P. Edwards, Y. Xu, F. Li, C.-T. Dinh, M. Zhong, Y. Lou, D. Wu, L.-J. Chen, E. H. Sargent, D. Sinton, *Nat. Catal.* **2019**, *2*, 251–258.
- [29] S. H. Lee, I. Sullivan, D. M. Larson, G. Liu, F. M. Toma, C. Xiang, W. S. Drisdell, *ACS Catal.* **2020**, *10*, 8000–8011.
- [30] H. H. Heenen, H. Shin, G. Kastlunger, S. Overa, J. A. Gauthier, F. Jiao, K. Chan, *Energy Environ. Sci.* **2022**, *15*, 3978–3990.
- [31] X. Wang, P. Ou, A. Ozden, S.-F. Hung, J. Tam, C. M. Gabardo, J. Y. Howe, J. Sisler, K. Bertens, F. P. García de Arquer, R. K. Miao, C. P. O'Brien, Z. Wang, J. Abed, A. S. Rasouli, M. Sun, A. H. Ip, D. Sinton, E. H. Sargent, *Nat. Energy* **2022**, *7*, 170–176.
- [32] H. H. Heenen, H. S. Pillai, K. Reuter, V. J. Bukas, *Nat. Catal.* **2024**, *7*, 847–854.
- [33] L. Wang, S. Nitopi, A. B. Wong, J. L. Snider, A. C. Nielander, C. G. Morales-Guio, M. Orazov, D. C. Higgins, C. Hahn, T. F. Jaramillo, *Nat. Catal.* **2019**, *2*, 702–708.
- [34] J. Jin, J. Wicks, Q. Min, J. Li, Y. Hu, J. Ma, Y. Wang, Z. Jiang, Y. Xu, R. Lu, G. Si, P. Papangelakis, M. Shakouri, Q. Xiao, P. Ou, X. Wang, Z. Chen, W. Zhang, K. Yu, J. Song, X. Jiang, P. Qiu, Y. Lou, D. Wu, Y. Mao, A. Ozden, C. Wang, B. Y. Xia, X. Hu, V. P. David, et al., *Nature* **2023**, *617*, 724–729.
- [35] W. Luc, X. Fu, J. Shi, J.-J. Lv, M. Jouny, B. H. Ko, Y. Xu, Q. Tu, X. Hu, J. Wu, Q. Yue, Y. Liu, F. Jiao, Y. Kang, *Nat. Catal.* **2019**, *2*, 423–430.
- [36] Y. Ji, Z. Chen, R. Wei, C. Yang, Y. Wang, J. Xu, H. Zhang, A. Guan, J. Chen, T.-K. Sham, J. Luo, Y. Yang, X. Xu, G. Zheng, *Nat. Catal.* **2022**, *5*, 251–258.
- [37] C. S. Cha, *Porous Electrode in Introduction to the Kinetics of Electrode Processes*, Science Press, Beijing, **2002**, pp. 345–377.
- [38] R. L. Frost, W. N. Martens, L. Rintoul, E. Mahmutagic, J. T. Kloprogge, *J. Raman Spectrosc.* **2002**, *33*, 252–259.
- [39] I. V. Chernyshova, P. Somasundaran, S. Ponnurangam, *Proc. Natl. Acad. Sci. USA* **2018**, *115*, E9261–E9270.
- [40] J. Gao, H. Zhang, X. Guo, J. Luo, S. M. Zakeeruddin, D. Ren, M. Grätzel, *J. Am. Chem. Soc.* **2019**, *141*, 18704–18714.
- [41] J. Peng, B. Chen, Z. Wang, J. Guo, B. Wu, S. Hao, Q. Zhang, L. Gu, Q. Zhou, Z. Liu, S. Hong, S. You, A. Fu, Z. Shi, H. Xie, D. Cao, C.-J. Lin, G. Fu, L.-S. Zheng, Y. Jiang, N. Zheng, *Nature* **2020**, *586*, 390–394.
- [42] J. Chen, M. Aliasgar, F. B. Zamudio, T. Zhang, Y. Zhao, X. Lian, L. Wen, H. Yang, W. Sun, S. M. Kozlov, W. Chen, L. Wang, *Nat. Commun.* **2023**, *14*, 1711.
- [43] W. Ma, S. Xie, B. Zhang, X. He, X. Liu, B. Mei, F. Sun, Z. Jiang, L. Lin, Q. Zhang, B. Ren, G. Fu, X. Hu, Y. Wang, *Chem* **2023**, *9*, 2161–2177.
- [44] X. Liu, W. Zhou, Y. Yang, K. Cheng, J. Kang, L. Zhang, G. Zhang, X. Min, Q. Zhang, Y. Wang, *Chem. Sci.* **2018**, *9*, 4708–4718.
- [45] J. Su, D. Wang, Y. Wang, H. Zhou, C. Liu, S. Liu, C. Wang, W. Yang, Z. Xie, M. He, *ChemCatChem* **2018**, *10*, 1536–1541.
- [46] F. Jiao, X. Pan, K. Gong, Y. Chen, G. Li, X. Bao, *Angew. Chem. Int. Ed.* **2018**, *57*, 4692–4696.
- [47] W. Zhou, J. Kang, K. Cheng, S. He, J. Shi, C. Zhou, Q. Zhang, J. Chen, L. Peng, M. Chen, Y. Wang, *Angew. Chem. Int. Ed.* **2018**, *57*, 12012–12016.
- [48] J. Andraos, A. J. Kresge, *Can. J. Chem.* **2000**, *78*, 508–515.
- [49] G. Kresse, J. Furthmüller, *Comput. Mater. Sci.* **1996**, *6*, 15–50.
- [50] P. E. Blöchl, *Phys. Rev. B* **1994**, *50*, 17953.
- [51] J. P. Perdew, J. A. Chevary, S. H. Vosko, K. A. Jackson, M. R. Pederson, D. J. Singh, C. Fiolhais, *Phys. Rev. B* **1992**, *46*, 6671.
- [52] Y. Zhang, W. Yang, *Phys. Rev. Lett.* **1998**, *80*, 890.
- [53] H.-F. Wang, Z.-P. Liu, *J. Am. Chem. Soc.* **2008**, *130*, 10996–11004.
- [54] C. Guo, X. Tian, X. Fu, G. Qin, J. Long, H. Li, H. Jing, Y. Zhou, J. Xiao, *ACS Catal.* **2022**, *12*, 6781–6793.
- [55] J. K. Nørskov, J. Rossmeisl, A. Logadottir, L. Lindqvist, J. R. Kitchin, T. Bligaard, H. Jónsson, *J. Phys. Chem. B* **2004**, *108*, 17886–17892.
- [56] P.-P. Yang, X.-L. Zhang, F.-Y. Gao, Y.-R. Zheng, Z.-Z. Niu, X. Yu, R. Liu, Z.-Z. Wu, S. Qin, L.-P. Chi, Y. Duan, T. Ma, X.-S. Zheng, J.-F. Zhu, H.-J. Wang, M.-R. Gao, S.-H. Yu, *J. Am. Chem. Soc.* **2020**, *142*, 6400–6408.
- [57] T. T. H. Hoang, S. Ma, J. I. Gold, P. J. A. Kenis, A. A. Gewirth, *ACS Catal.* **2017**, *7*, 3313–3321.
- [58] W. Ma, S. Xie, T. Liu, Q. Fan, J. Ye, F. Sun, Z. Jiang, Q. Zhang, J. Cheng, Y. Wang, *Nat. Catal.* **2020**, *3*, 478–487.
- [59] R. Satthawong, N. Koizumi, C. Song, P. Prasassarakich, *Catal. Today* **2015**, *251*, 34–40.

- [60] W. Li, A. Zhang, X. Jiang, M. J. Janik, J. Qiu, Z. Liu, X. Guo, C. Song, *J. CO₂ Util.* **2018**, 23, 219–225.
- [61] M. Fujiwara, T. Satake, K. Shiokawa, H. Sakurai, *Appl. Catal. B Environ.* **2015**, 179, 37–43.
- [62] C. G. Visconti, M. Martinelli, L. Falbo, A. Infantes-Molina, L. Lietti, P. Forzatti, G. Iaquaniello, E. Palo, B. Picutti, F. Brignoli, *Appl. Catal. B Environ.* **2017**, 200, 530–542.
- [63] A. Ramirez, L. Gevers, A. Bavykina, S. Ould-Chikh, J. Gascon, *ACS Catal.* **2018**, 8, 9174–9182.
- [64] B. Endrődi, E. Kecsenovity, A. Samu, F. Darvas, R. V. Jones, V. Török, A. Danyi, C. Janáky, *ACS Energy Lett.* **2019**, 4, 1770–1777.
- [65] W. H. Lee, Y.-J. Ko, Y. Choi, S. Y. Lee, C. H. Choi, Y. J. Hwang, B. K. Min, P. Strasser, H.-S. Oh, *Nano Energy* **2020**, 76, 105030.
- [66] W. H. Lee, K. Kim, C. Lim, Y.-J. Ko, Y. J. Hwang, B. K. Min, U. Lee, H.-S. Oh, *J. Mater. Chem. A* **2021**, 9, 16169–16177.
- [67] L. Lin, X. He, X.-G. Zhang, W. Ma, B. Zhang, D. Wei, S. Xie, Q. Zhang, X. Yi, Y. A. Wang, *Angew. Chem. Int. Ed.* **2023**, 62, e202214959.
- [68] G. Zhang, B. Tan, D. H. Mok, H. Liu, B. Ni, G. Zhao, K. Ye, S. Huo, X. Miao, Z. Liang, X. Liu, L. Chen, Z. Zhang, W.-B. Cai, S. Back, K. Jiang, *Proc. Natl. Acad. Sci. USA* **2024**, 121, e2400898121.
- [69] J. Zhu, J. Li, R. Lu, R. Yu, S. Zhao, C. Li, L. Lv, L. Xia, X. Chen, W. Cai, J. Meng, W. Zhang, X. Pan, X. Hong, Y. Dai, Y. Mao, J. Li, L. Zhou, G. He, Q. Pang, Y. Zhao, C. Xia, Z. Wang, L. Dai, L. Mai, *Nat. Commun.* **2023**, 14, 4670.

Manuscript received: February 01, 2025

Revised manuscript received: February 26, 2025

Accepted manuscript online: March 07, 2025

Version of record online: March 18, 2025